

AIAA Aviation Forum and Exposition, 17 - 21 June 2019, Dallas, Texas

# A DNS Study to Investigate Turbulence Suppression in Rotating Pipe Flows

Jefferson Davis<sup>1</sup>\*, Sparsh Ganju<sup>1</sup>†, Neil Ashton<sup>2</sup>‡, Sean Bailey<sup>1</sup>§ and Christoph Brehm<sup>1</sup>¶

Department of Mechanical Engineering, University of Kentucky, Lexington, KY 40506, USA.

Department of Engineering Science, University of Oxford, UK.

Rotating and swirling turbulence comprises an important class of flows, not only due to the complex physics that occur, but also due to their relevance to many engineering applications, such as combustion, cyclone separation, mixing, etc. In these types of flows, rotation strongly affects the characteristics and structure of turbulence. However, the underlying turbulent flow phenomena are complex and currently not well understood. The axially rotating pipe is an exemplary prototypical model problem that exhibits these complex turbulent flow physics. By examining turbulent statistics, the physical mechanisms responsible for turbulence suppression are investigated. Direct numerical simulations are conducted at a bulk Reynolds number up to  $Re_D = 19,000$  with rotation numbers ranging from N = 0 to 3. Within the chosen range of Reynolds numbers, some Reynolds number dependence on the results was observed. Turbulent kinetic energy budgets and Reynolds stresses were computed for these flows to quantify the effects of rotation on the turbulent flow. It is found that rotation causes a reduction in production near the wall and an increase in dissipation in inner-scaled dissipation. Additionally, a small region of increased turbulent production was found near the center of the pipe flow.

#### I. Introduction

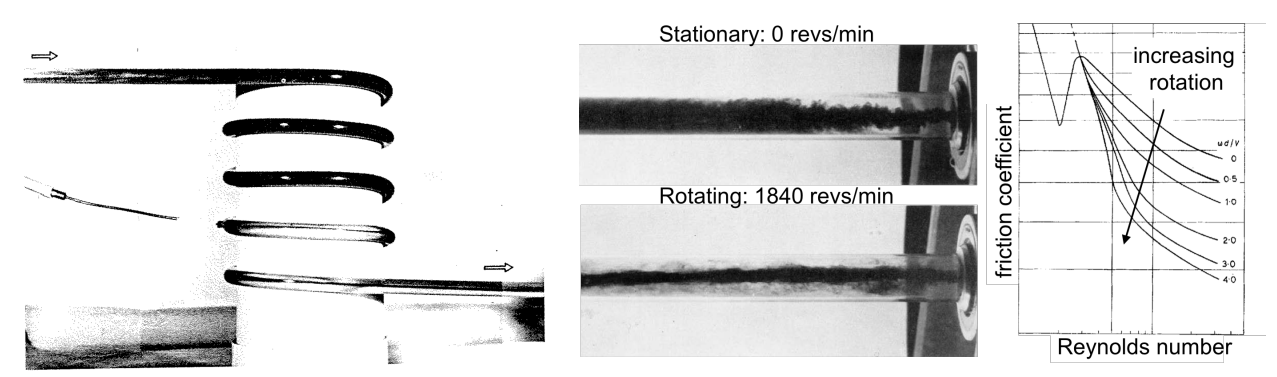


Fig. 1 Relaminarization visualized by dye injected into a turbulent pipe flow entering a coiled tube (left) and stationary/rotating pipe with dye entering on the right (middle). (right) Effect of rotation on friction coefficient. (Figs. adjusted from[1, 2])

Rotating and swirling turbulent flows are of high importance to the engineering community due to their prevalence in aerospace, industrial, and natural systems. In aerospace industries, wall-bounded rotating turbulence affects almost every aspect of flight, from swept wings and wing-tip vorticies to turbo-compressors. Despite the prevalence of these flows, little is known about the physical mechanisms responsible for some aspects of rotational turbulence. An interesting aspect which can occur when rotating a turbulent flow is the phenomenon known as turbulence suppression, which has been shown to cause reduction in drag at the wall[3–7], making the understanding of turbulence suppression highly valuable for engineering applications.

Turbulence suppression has been observed in notable experiments dating back to the 1960s[2] and some Direct Numerical Simulations (DNSs) of rotational pipe flows have been conducted at only relatively low Reynolds numbers[7–10]. However, the understanding of turbulence suppression remains limited to the identification of the basic physical

mechanisms responsible for inducing suppression. Axially rotating pipe flows provide an excellent prototypical case for examination of turbulence suppression, as these flows eliminate unnecessary complications introduced by complex geometry and can be realized effectively in both simulation and laboratory experiment. DNS of these flows was conducted in conjunction with experimental research currently underway at the University of Kentucky[11].

In experiments by Kikuyama *et al.*[4], velocity distributions and hydraulic loss were obtained for downstream positions in rotational flows at Reynolds numbers up to Re = 50,000, where  $Re = U_b D/\nu$ , in a domain of L = 160D, and found that these flows reach a fully-developed state within 120D. In these experiments, increasing rotation was shown to correspond to a reduction in friction coefficient and the relationship between Richardson number and mixing length established by Bradshaw[12] was verified. Depending on rotation rate, it may be relevant to describe a rotating pipe flow as either: 1) a pipe flow regime with an additional axial rotation, defined by  $Re = U_b D/\nu$  or 2) a rotating flow inside a cylinder (solid body rotation) with an additional cross flow, defined by  $Re_w = U_w D/2\nu$ , where  $U_w$  is the velocity of the wall. It can be seen that the rotation number, N, where  $N = \Omega D/2U_b$ , can be equivalently defined as a ratio between these two Reynolds numbers. The competition for dominance between these two regimes was shown in experiments by Nishibori *et al.*[5] where it was found that a rotating laminar layer close to the wall of axially rotating flows surrounds the non-rotating turbulent core in the inlet region (20-60 diameters from the entrance), this laminarization destabilizes downstream as the core begins to rotate, resulting in turbulent bursts which extend into the near-wall region. Reich and Beer[6] examined flows from Re = 5,000 to 50,000 with rotation rates up to N = 5. In these experiments, effects of rotation on mixing length were examined on a domain of L = 130D, reduction in friction coefficient was found and a broad connection between turbulence suppression and the centrifugal force was established[6].

While numerous experimental studies have been conducted regarding rotating pipe flows, DNS of these flows have been very limited. Simulations of axially rotating and non-rotating pipe flow were conducted by Feiz et al. [7] at Re = 4,900 and 7,400, as well as LES at Re = 20,000. Reduction in skin friction was found with increasing N and was shown to become more significant at larger Reynolds numbers, as well as a decrease in streamwise velocity profiles with increasing Re[7]. In studies by Orlandi & Fatica[8] and Orlandi & Ebstein[9], flows up to Re = 4,900 and rotation numbers up to N = 10 were analyzed. By examining two-point velocity correlations, it was found that drag reduction is related to the widening of streaks and changes to vortical structures in the near wall region. The observations by Orlandi & Fatica[8] indicate that understanding the near-wall region of rotating flows is paramount to understanding turbulence suppression. Due to the difficulty in taking experimental measurements in this region, it is clear that higher Reynolds number DNS are required to gain insight into the complex problem of turbulence suppression. With this in mind, simulations were conducted at Reynolds numbers Re = 5,300, 11,700, and 19,000 and rotation numbers in the range N = 0-3. These studies build on previous work presented by Davis et al. [13, 14] and concurrent work by Brehm et al. [15]. Some complimentary work on RANS modeling in rotating pipe flows using the present DNS data for comparison are presented in a companion paper by Ashton et al. [16]. This modeling effort builds off initial work by Ashton and Stoellinger [17] on the Elliptic Blending Reynolds Stress Model as a means to better capture turbulence suppression in axially rotating pipe flow.

This paper is organized as follows: Section II discusses the chosen solver for these simulations, computational domain considerations, and simulation requirements; mean velocity profiles are compared in Section III.A; Section III.B presents analysis of the effects of rotation on Reynolds stresses; turbulent kinetic energy is examined in Section III.C, and turbulent kinetic energy budgets are analyzed in Section III.D.

# **II. Computational Methods**

Simulations were conducted using the spectral element solver Nek5000, developed by Fischer *et al*[18]. Nek5000 is a higher-order accurate, open source, spectral element solver used to solve the incompressible Navier-Stokes equations and is well-known for its (spectral) accuracy, favorable dispersion properties, and efficient parallelization[19]. The spectral element method is based on a weighted-residual approach for spatial discretization. For parallel computations, Nek5000 utilizes the message passing interface (MPI) protocol and has shown excellent scaling characteristics on HPC systems — making it well-suited for large-scale turbulence flow computations. The mesh is comprised of hexahedral elements with the solution being composed of  $N^{th}$ -order tensor product polynomials within each element. Local lexicographical ordering within each macro element, as well as the need to evaluate only  $O(EN^4)$  discrete operators, which typically have  $O(EN^6)$  non-zeros, leads to the cache and vectorization efficiency[18]. A semi-implicit time-integration scheme is used where the viscous terms of the Navier-Stokes equations are treated implicitly with third-order backward differentiation (BDF3) and the nonlinear advection terms are explicitly extrapolated in time with third-order accuracy.

Nek5000 minimally uses external libraries to increase compile speed, and matrix operations are implemented

in assembler code  $M\times M$  routines to speed up computations. Furthermore, Nek5000 tests each of the three parallel algorithms at the beginning of each run to determine which behaves optimally — thus parallelism is automatically tuned for each machine[18]. The algebraic multi-grid (AMG) solver was chosen throughout this work from the different pressure Poisson solvers available in Nek5000.

The choice of the domain size such that a fully developed flow can be obtained is an important issue both for numerical simulations and experiments. Flow visualizations by Nishibori et al.[5] showed that coherent flow structures form in the center of the pipe at high rotation rates. Thus, to avoid a negative impact of the domain size on the computational results, it has to be ensured that the fluctuating velocities measured at two locations separated by a streamwise distance of O(L) are uncorrelated. Orlandi and Fatica[8] found that a domain size of L/D = 7.5 for Re = 4,900 and N = 2 is sufficient to resolve the largest flow structures within the domain. Khoury et al.[19] showed a domain size of L/D = 12.5 to be sufficient for pipe flows at Reynolds numbers up to Re = 37,700, being the more conservative estimate, this domain was chosen for the current simulations. As shown in Fig. 2, periodic boundary conditions were used at the inflow and outflow of the domain to allow the simulations to reach a fully developed state.

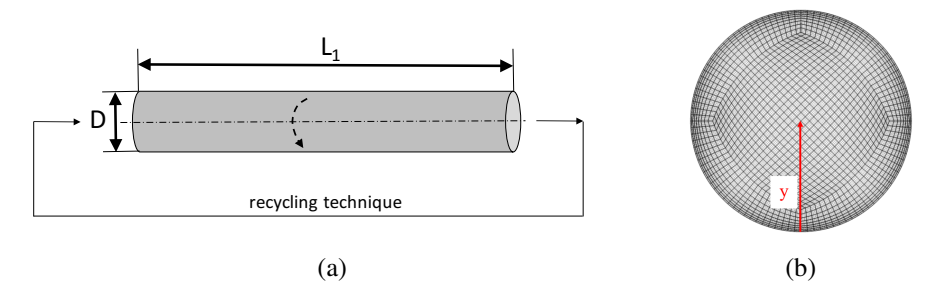


Fig. 2 (a) Simulation domain and (b) mesh cross-section for the fully developed turbulent flow simulations.

The different grid sizes,  $N_{\Delta x}$ , are provided in Table 1. Sufficient temporal and spatial resolution is required to thoroughly study the intricate nature of turbulence, turbulence suppression and relaminarization. The computational mesh shown in Fig. 2b. It was chosen to resolve the wide range of different turbulent scales. The radial, azimuthal and streamwise grid spacings are reported in  $y^+$ -units and different ranges are provided because the mesh varies within the computational domain. Note that the friction factor (or skin friction values) used to calculate the grid spacings in  $y^+$ -units were obtained from non-rotating turbulent pipe flow simulations. The provided grid spacings in  $y^+$ -units are conservative estimates for the rotating pipe flow simulations because the skin friction values were expected to be lower for a rotating pipe due to the relaminarization process.

Re	f	$\Delta r^+/\Delta R\Theta^+/\Delta z^+$	$N_{\Delta x} \times 10^6$	$\Delta t$	$N_{\Delta t}$	ft	fa
5,300	0.0375	0.14-4.4/1.5-4.5/3.0-9.9	20	0.00150	220,000	26.5	20
11,700	0.0300	0.16-4.7/1.5-5.0/3.0-9.9	120	0.00085	265,000	18	11.5
19,000	0.0270	0.15-4.5/1.5-4.8/3.0-10.	440	0.00053	400,000	14	6.5

Table 1 Details of turbulent pipe flow simulations assuming a streamwise extent of 15D, where Re refers to Reynolds number,  $f = 8u_{\tau}^2/U_b^2$  is the friction factor,  $N_{\Delta x}$  is the number of grid points in the computational domain,  $\Delta t$  is the chosen timestep,  $N_{\Delta t}$  is the number of total timesteps, and  $\Delta r^+$ ,  $\Delta R\Theta^+$  and  $\Delta z^+$  are the grid spacings measured in  $y^+$ -units. Note that for the grid spacings different ranges are provided because the mesh is non-uniform. The flow through time is ft, and, finally, fa is the number of flow throughs over which temporal averaging was conducted.

Since the convective terms of the incompressible Navier-Stokes equations are treated with an explicit time-integration scheme, to allow for a stable numerical solution the non-dimensional timestep,  $\Delta t$ , corresponds to a CFL number of less than 1. The timesteps provided in Table 1 were chosen to ensure CFL=0.75. To obtain fully-converged turbulent statistics we require a total compute time of at least ten flow through times which includes an initial transient. The total number of timesteps,  $N_{\Delta t}$ , reported in Table 1 are based on flow through times providing sufficient accuracy in the turbulent statistics that can be obtained from the simulations, where the number of flow throughs during which averaging occurred is given by fa in Table 1.

# III. Results

To gain an understanding of rotational effects in pipe flows; mean profiles, Reynolds stresses, turbulent kinetic energy, and turbulent kinetic energy budgets were computed for each case. Turbulent statistics were obtained by computing time averages at each point at run-time followed by spatial averaging in the streamwise and azimuthal directions. Values were directly averaged in the streamwise direction, as the computational domain is uniform in this direction, but interpolation onto a radially uniform grid was required for azimuthal averaging. Values which have been spatially and temporally averaged in this manner are denoted with  $<\cdot>$ .

To better understand turbulence suppression, a rigorous, quantifiable metric for measuring the degree of suppression in a flow is needed. However, previous studies have yet to identify such a metric, with many studies using qualitative features and some studies mentioning the existence of the phenomenon without classifying it in any way. One common quantification of turbulence suppression is the measure of wall friction, but friction is completely determined by the state of the flow at the wall, and does not directly characterize the flow as a whole. This metric should: 1. indicate the existence of turbulence suppression in flows that contain the classical flow features associated with suppression, e.g. friction reduction and a more parabolic mean profile; 2. be readily computable from turbulent statistics; and 3. should be a sensible measure of turbulence. To identify this metric, turbulent kinetic energy is examined in Section III.C as well as mean profiles and drag reduction in Section III.A. Turbulent kinetic energy budgets are examined in Section III.D, with an emphasis on examining the influences of the two competing regimes, *i.e.* the pipe flow regime and the flow inside a rotating cylinder regime, in terms of the budget equation.

# A. Mean Velocity Profiles

Streamwise mean velocity profiles were calculated for each case and are presented in Fig. 3 normalized by the bulk velocity. From Fig. 3a, it can be seen that the dependence on Reynolds number is small, and that the profile is dominated by rotation rate dependence. This obsevation agrees well with experimental data by Kikuyama *et al.*[4]. The reduction in mean streamwise velocity towards the wall provides a strong indication of a reduction in mixing within the flow, whereby high velocity flow remains concentrated towards the center of the flow. This results in a mean velocity profile which appears to approach the laminar profile as the rotation rate is increased, which has been used in prior works as an indication of turbulence suppression.

Normalizing the mean streamwise velocity with  $u_{\tau}$  yields the inner-scaled value, which is presented in Fig. 3b. Here, a significant deviation from the log-law is evident in rotational flow, with high dependence on N.

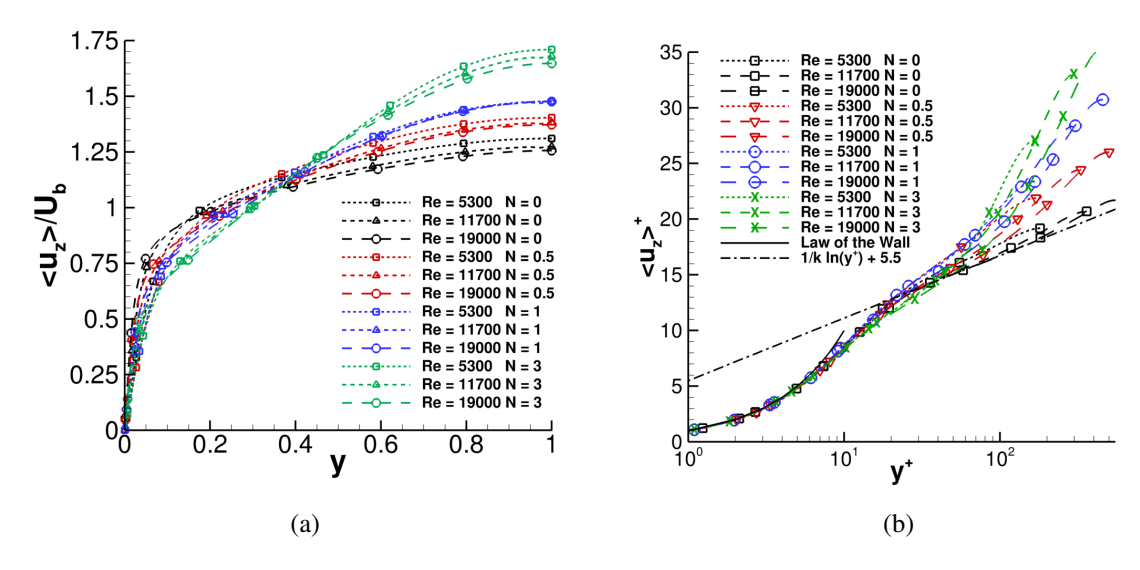


Fig. 3 Mean streamwise velocity profiles for all Reynolds numbers (a) normalized with bulk velocity  $U_b$  and (b) in inner scaling.

Similar trends to those found in mean streamwise velocity are present in mean azimuthal velocity. Mean azimuthal velocity profiles for Re = 19,000 are shown in Fig. 4a normalized by velocity at the wall,  $U_w$  in an inertial (laboratory) reference frame. Swirl is shown in Fig. 4b, here in a reference frame rotating with the pipe. The location of the peak in

swirl is unaffected by N, though the magnitude of the peak does show significant dependence on rotation. Reynolds number dependence is seen in both magnitude and location of the peak, with the peak being shifted towards the center of the flow for Re = 5,300.

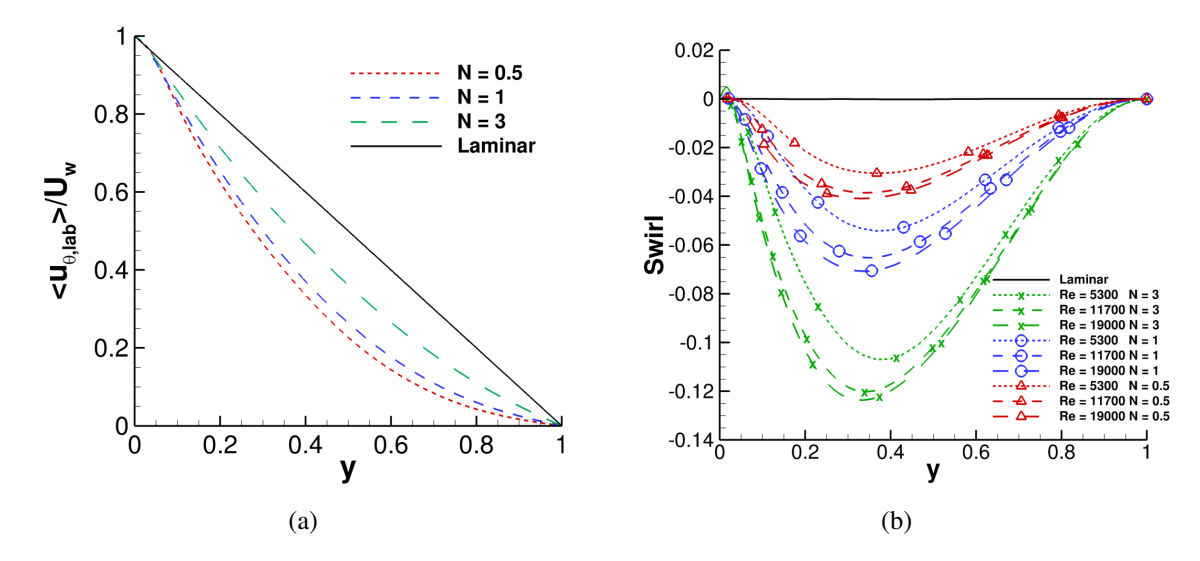


Fig. 4 (a) Mean azimuthal velocity (non-rotating reference frame) profiles normalized by the velocity of the wall for Re = 19,000 and (b) a comparison of swirl profiles.

The friction Reynolds number, given by  $Re_{\tau} = u_{\tau}D/v$ , reduces significantly for low rotation rates followed by a slight reduction for N=3, as shown in Fig. 5. By normalizing  $Re_{\tau}$  with  $Re_{\tau,0}$ , which is the friction Reynolds number for the non-rotational flow at a given bulk Reynolds number, as shown in Fig. 5, the reduction in friction Reynolds number can be more clearly visualized. The dependence of this reduction on bulk Reynolds number is initially quite significant, with the percentage of reduction more than doubling from Re=5,300 to Re=11,700 for N=1 and 3. As the Reynolds number is increased further, however, the impact on drag reduction becomes less significant. An abrupt change in the efficiency of friction reduction with increasing N can also be seen, with moderate rotation numbers N = 1 showing significant reduction in N = 1 results in only a modest additional decrease.

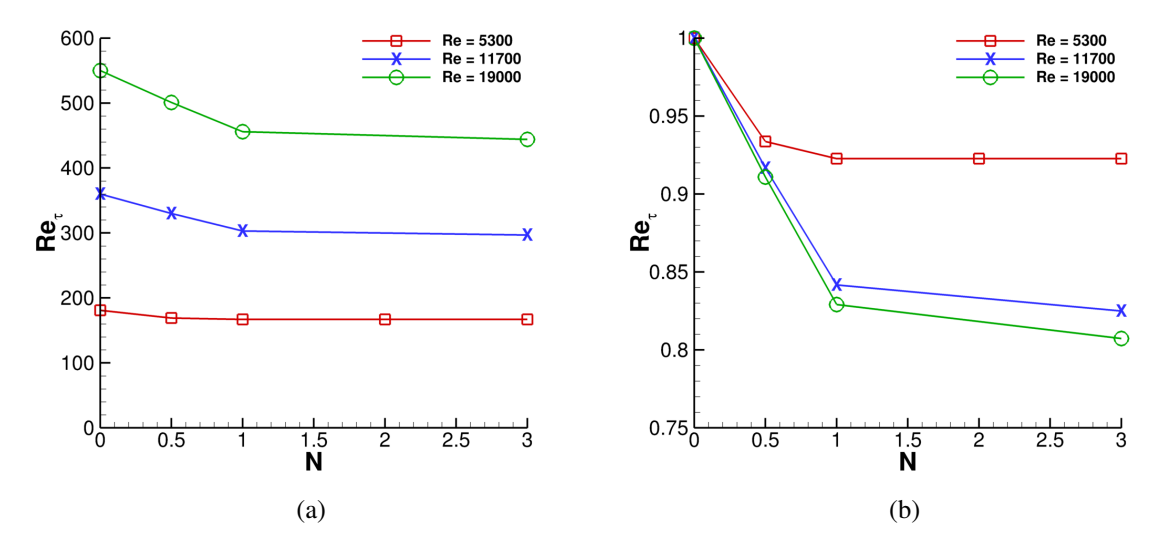


Fig. 5 (a) Comparison of friction Reynolds number for different rotation Numbers. (b) Relative reduction of friction Reynolds number (normalized by non-rotating friction Reynolds number).

#### **B. Reynolds Stresses**

Reynolds stresses were evaluated in a streamline-aligned coordinate system offset from the streamwise, or z-direction, by  $\theta_s$ , which is given by:

$$\theta_s = \cos^{-1}\left(\frac{U_z}{\sqrt{U_z^2 + U_{\theta,lab}^2}}\right). \tag{1}$$

The profiles of this mean streamline angle  $\theta_s$  are shown in Fig. 6, where it can be seen that away from the wall, all profiles begin to organize depending on rotation rate N due to the high dependence of both  $U_z$  and  $U_\theta$  on N as evidenced in Fig. 3 and Fig. 4. Close to the wall, mean velocity profiles adhere to the law of the wall, resulting in a sorting of  $\theta_s$  by Re as seen in the inset for Fig. 6.

The effects of rotation on the Reynolds stress aligned with the streamline direction,  $\langle u_1 u_1 \rangle^+$ , where + denotes traditional innerscaling with  $u_{\tau}^2$ , are clearly visible in Fig. 7. Rotation causes a drastic reduction in the near-wall peak in  $\langle u_1u_1 \rangle$ , while also leading to the formation of a separate peak away from the wall which grows with increasing rotation rate. The reduction in the near-wall peak is simply due to the realignment of the streamline coordinate system from the rotating to non-rotating case, while the formation of the central peak does not appear to depend on the chosen coordinate system. The interested reader is referred to the Appendix for Reynolds stresses in (the  $r,z,\theta$ ) coordinate system, as well as validation with low-Re data from the literature. This central peak does, however, show dependencies on Reynolds number, with diminishing intensity as the Reynolds number increases contrary to the behavior of the near-wall peak, which shows a very mild increase with increasing Reynolds number for the non-rotating case.

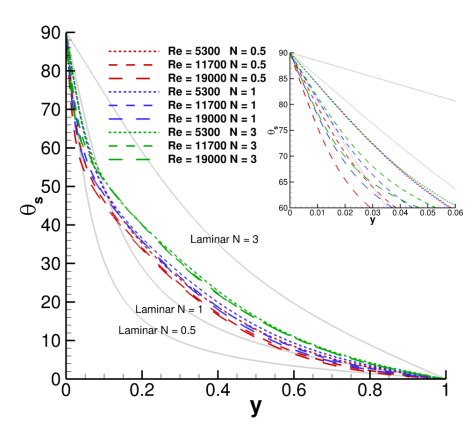


Fig. 6 Streamline angle  $\theta_s$  between streamline and streamwise directions.

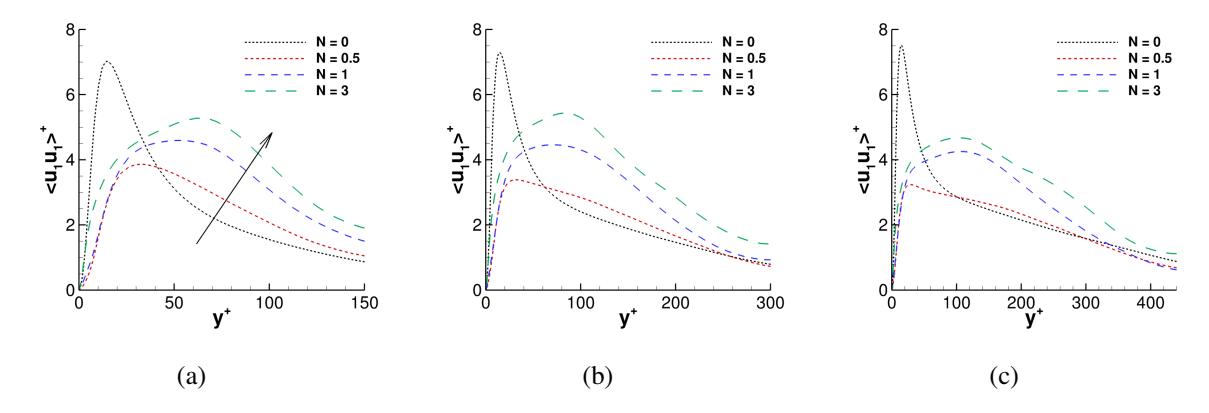


Fig. 7 Normal Reynolds stress aligned with the streamline direction normalized by  $u_{\tau}^2$  for (a) Re = 5,300, (b) Re = 11,700, and (c) Re = 19,000.

The  $\langle u_2 u_2 \rangle^+$  Reynolds stress is aligned in the radial direction

and experiences a general increase with rising N which may be caused by an increase in forcing in this direction from the centrifugal force. The component of the Reynolds stress tensor aligned with the third direction (i.e. mutually orthogonal to the streamline and radial directions),  $< u_3 u_3 >^+$  also shows the formation of a second peak at the same location as the peak observed in  $< u_1 u_1 >^+$ , indicating a transfer in energy in the fluctuations along the first and third directions. The near-wall peak present in  $< u_1 u_1 >^+$  for N = 0 is now visible in  $< u_3 u_3 >^+$ , as this third direction aligns with the direction of azimuthal forcing at the wall.

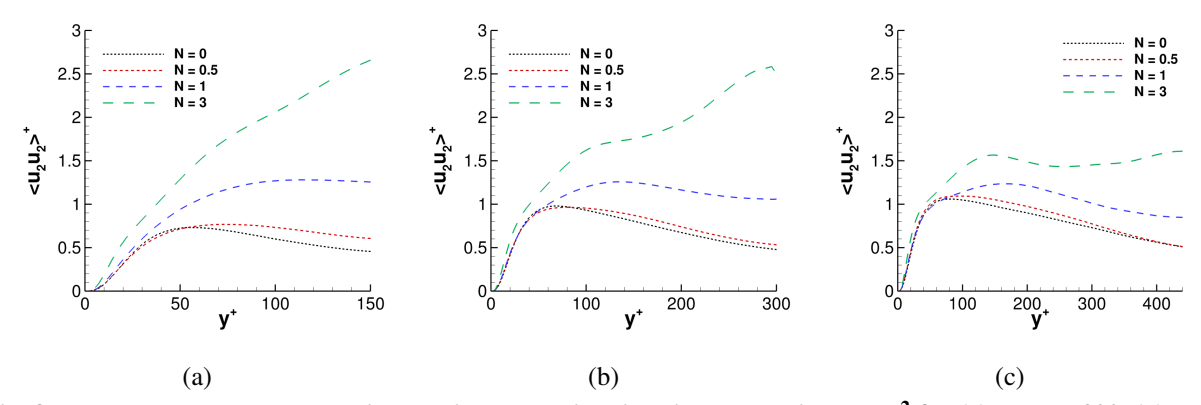


Fig. 8 Normal Reynolds stress aligned with the radial direction normalized by  $u_{\tau}^2$  for (a) Re = 5,300, (b) Re = 11,700, and (c) Re = 19,000.

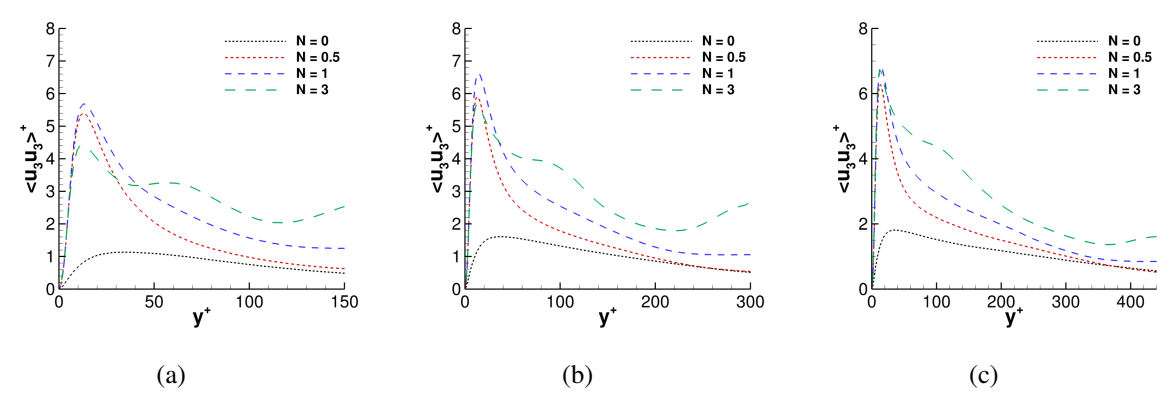


Fig. 9 Normal Reynolds stress aligned with the third axis (i.e. orthogonal to the streamline and radial directions.) normalized by  $u_{\tau}^2$  for (a) Re = 5,300, (b) Re = 11,700, and (c) Re = 19,000.

#### C. Turbulent Kinetic Energy

Turbulent kinetic energy, k, describes the energy present in the fluctuating part of the flow and is, therefore, a sensible candidate for quantifying turbulence suppression. Before defining a metric to measure suppression, however, an appropriate normalization for k must be selected. To determine this metric, k for each flow case was analyzed to determine a normalization which is readily obtainable, physically sensible, and conforms to previous definitions of turbulence suppression.

Turbulent kinetic energy was calculated using:

$$k = \frac{1}{2} \left( \langle u_1 u_1 \rangle + \langle u_2 u_2 \rangle + \langle u_3 u_3 \rangle \right) \tag{2}$$

and is shown in inner-scaling for each case in Fig. 10a-c. It is noted that the peak in  $k^+$  near the wall experiences a slight increase with increasing N and narrowing with additional Re; additionally, there is a marked increase in  $k^+$  towards the pipe centerline. The location of the near-wall peak is unaffected by Re, remaining constant at  $y^+ \approx 17$ , while the peak away from the wall, formed at higher rotation rates, does show Reynolds number dependence in both location and magnitude, and corresponds to a peak in production (see Fig. 14). At first glance, turbulence appears to be enhanced by rotation in this scaling, which does not align with the current conception of turbulence suppression. Additionally, much of the increase in k is concentrated towards the center of the flow, and, therefore, contributes less to the overall turbulence. By multiplying k with r and normalizing by  $u_\tau^2 D$ , an inner-scaling for turbulent kinetic energy is arrived at that accounts for the integral of k in the azimuthal direction, and, therefore, represents the contribution in the integrand for the total turbulent kinetic energy, TKE. In this normalization, shown in Fig. 10d-f, it can be seen that the contribution to the total turbulent kinetic energy due to the increase in  $k^+$  away from the wall is far less than it appears to be in Fig. 10a-c, though this normalization still shows an apparent increase in turbulent kinetic energy with rotation.

By normalizing k with  $U_b^2$ , a decrease in the near-wall peak is evident with increasing rotation rate as seen in Fig. 12a-c. The peak formed away from the wall also shows significant Reynolds number dependence, reducing drastically

with increasing Re. As the Reynolds number increases, the effect of rotation on k toward the center of the flow become less significant while the decrease in the inner peak becomes more significant.

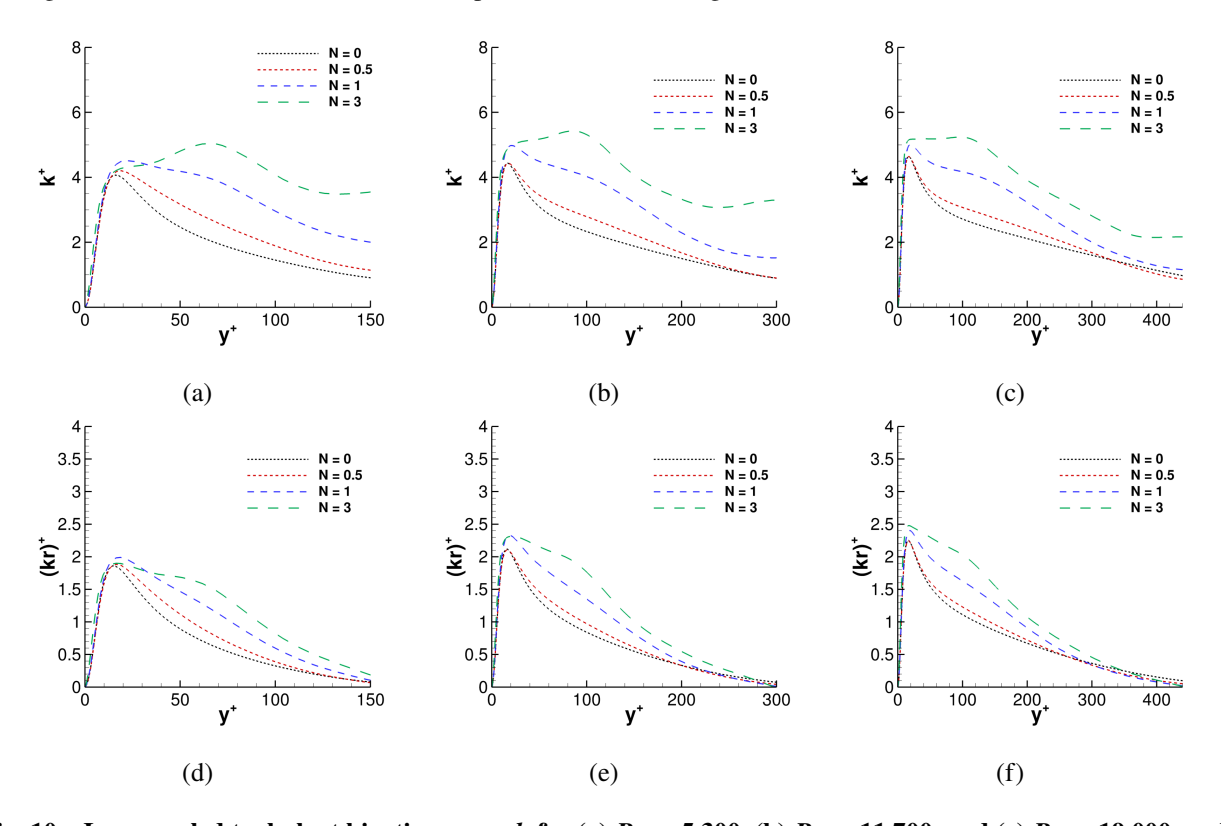


Fig. 10 Inner-scaled turbulent kinetic energy k for (a) Re = 5,300, (b) Re = 11,700, and (c) Re = 19,000, and inner-scaled turbulent kinetic energy multiplied with radial position for (d) Re = 5,300, (e) Re = 11,700, and (f) Re = 19,000.

Using a similar process to the one applied to  $k^+$ , turbulent kinetic energy is multiplied with r to compensate for the integrand and normalized using  $U_b^2D$  to obtain values that account for integration over the cross-sectional area. This normalization is presented in Fig. 12d-f and a reduction in total turbulent kinetic energy can now be seen for N = 0.5 at Reynolds numbers of 11,700 and 19,000. The second peak is significantly diminished, as fluctuations toward the center of the flow contribute less to the overall turbulent kinetic energy of the flow. The total turbulent kinetic energy integrated over the cross sectional area of the pipe is presented in Fig. 11 divided by the total turbulent kinetic energy for the non-rotating case. The percentage increase in TKE with N shows a strong dependence on Reynolds number, decreasing significantly with increasing Re. TKE at Re =5,300 N = 1, for example, is 32% higher than the non-rotating case, while TKE for Re = 19,000 at the same rotation number shows an increase of less than 2%.

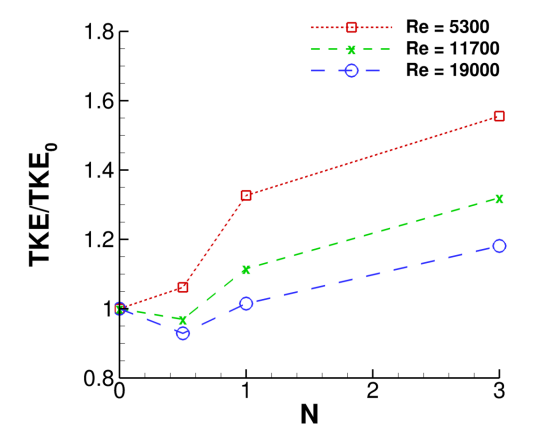


Fig. 11 Change in total turbulent kinetic energy.

By normalizing with  $U_b^2$  only a slight suppression in turbulence is seen for N=0.5, and only for sufficiently high Reynolds numbers. Applying this normalization, however, fails to account for the total kinetic energy available in the mean flow. The rotational component of the mean velocity becomes more significant as rotation rate increases, and it is, therefore, much more sensible to normalize by the total mean kinetic energy  $U_b^2 + U_\theta^2$ . In this new normalization, suppression of turbulence is much more pronounced, with the increase towards the center of the flow now showing

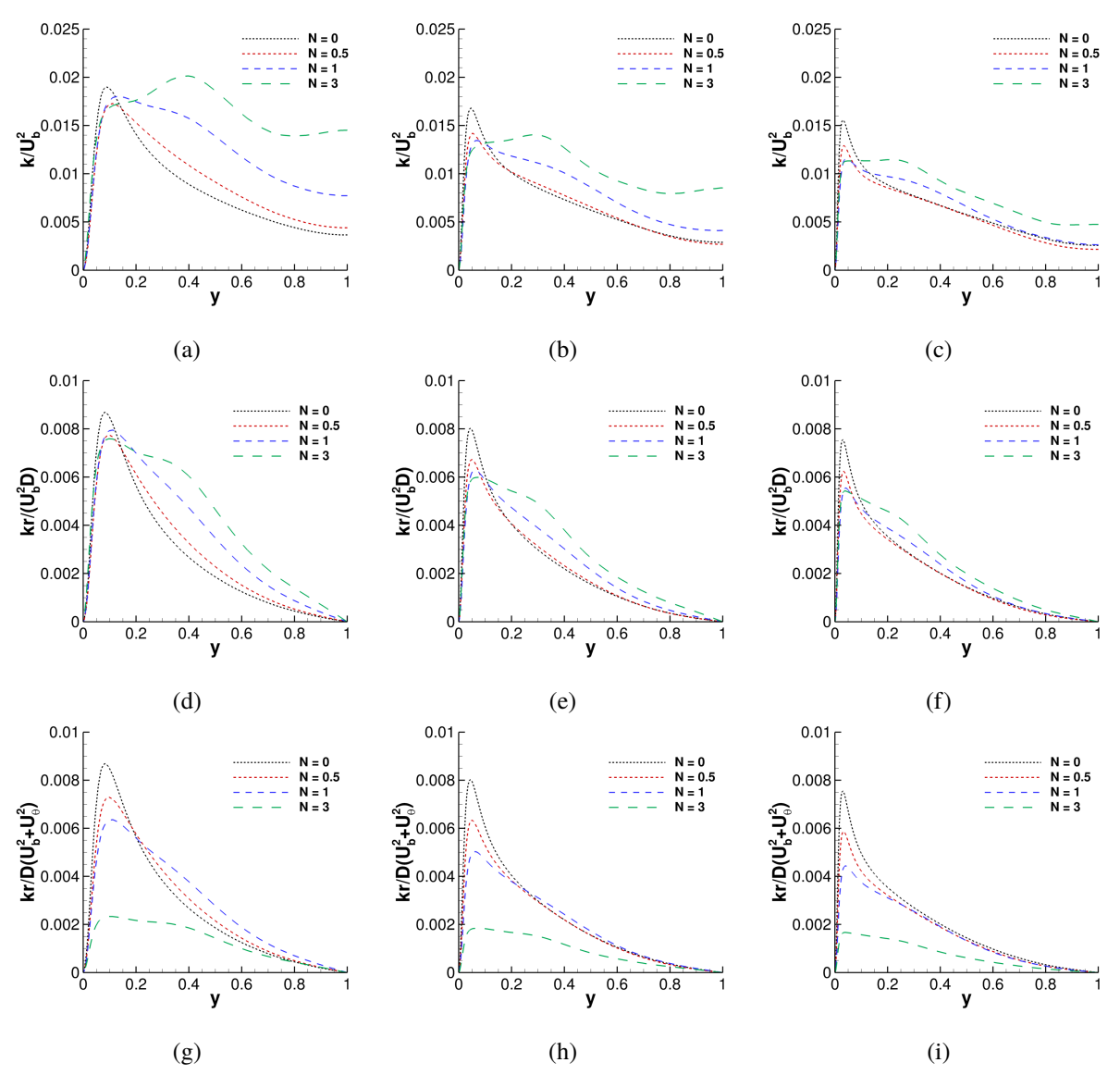


Fig. 12 Turbulent kinetic energy normalized by bulk velocity squared for (a) Re = 5,300, (b) Re = 11,700, and (c) Re = 19,000. Turbulent kinetic energy multiplied by radial position and normalized by  $U_b^2D$  is shown for (d) Re = 5,300, (e) Re = 11,700, and (f) Re = 19,000. Normalization by the total mean kinetic energy is shown for (g) Re = 5,300, (h) Re = 11,700, and (i) Re = 19,000

significant reduction from traditional scaling, as seen in Fig. 12j-l. It is also notable that this increase diminishes with increasing Reynolds number, and is completely absent in the Re=19,000 case, where all rotation rates now show suppression of turbulence.

Looking at the total value for TKE integrated over the cross section in Fig. 13, this normalization now shows reduction in TKE for all cases at sufficiently high Reynolds number. The only case now showing an excitation of total turbulent kinetic energy being Re = 5,300 N = 1. Previous descriptions of turbulence suppression relied on either a qualitative definition or an evaluation of drag at the wall. While drag measurements provide a way to quantitatively measure the effects of rotation on the flow, it is not a good measure for turbulence suppression. These types of measures only describe the state of the

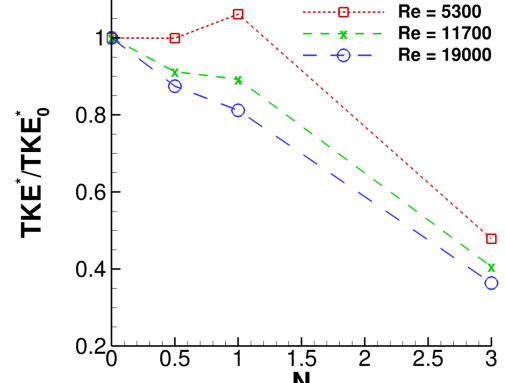


Fig. 13 Ratio of total turbulent kinetic energy normalized by mean kinetic energy to that of the non-rotating case.

flow near the wall, and fail to account for the characteristics of turbulence in the flow. The ratio of total turbulent kinetic energy to mean kinetic energy better describes the amount of turbulence in the flow, making this ratio much better suited as a metric for quantifying turbulence suppression.

# D. Turbulent Kinetic Energy Budgets

Just as turbulent kinetic energy is important in the quantification of turbulence suppression, an understanding of the turbulent kinetic energy budgets aids in understanding the mechanisms which generate or dissipate turbulence. Two competing extreme flow regimes are the pipe flow, characterized by Re, and rotating flow inside a cylinder (solid body rotation), characterized by  $Re_w$ . The rotation number N essentially represents a ratio of these two Reynolds numbers.

The turbulent kinetic energy budget equation given by Eqn. (3) provides a description of the change in k due to production of k from the mean flow, dissipation by molecular forces, and transfer by convection and diffusion.

$$\underbrace{\frac{\partial k}{\partial t}}_{\text{Rate of change of } k} = -\underbrace{\left\langle u_i' u_j' \right\rangle \frac{\partial \langle u_i \rangle}{\partial x_j}}_{\text{Production}} - \underbrace{\left\langle \varepsilon \right\rangle}_{\text{Turbulent dissipation}} - \underbrace{\left\langle k \right\rangle \langle u_j \right\rangle}_{\text{Convection by meanflow}} + \underbrace{\left\langle u_j' \left(k + \frac{p}{\rho}\right) \right\rangle}_{\text{Diffusion}} - \nu \underbrace{\left\langle u_i' \left(\frac{\partial u_i'}{\partial x_j} + \frac{\partial u_j'}{\partial x_i}\right)\right\rangle}_{\text{Diffusion}} \right\}. \tag{3}$$

Transfer of turbulent energy

In fully developed turbulence, the left hand side becomes zero, as well as the convection term, resulting in a balance between production P, dissipation  $\epsilon$ , and diffusion. Turbulent kinetic energy diffusion is described by three physical mechanisms: viscous diffusion, VD; turbulent diffusion, TD; and pressure diffusion, PD, given by Eqn. (4), (5), and (6), respectively,

$$VD = \frac{\partial}{\partial x_{i}} \left( \left\langle u_{j}^{'} k \right\rangle \right), \tag{4}$$

$$TD = \frac{\partial}{\partial x_j} \left( v \left( u_i^{'} \left( \frac{\partial u_i^{'}}{\partial x_j} + \frac{\partial u_j^{'}}{\partial x_i} \right) \right) \right), \text{ and}$$
 (5)

$$PD = \frac{\partial}{\partial x_j} \left( \left\langle u_j' \frac{P}{\rho} \right\rangle \right). \tag{6}$$

A reduction in peak production is observed with increasing rotation number as shown in Fig. 14a-c. At the lowest Reynolds number, Re = 5,300, the peak takes on a similar value for all rotation rates, however, as the Reynolds number is increased, a clear trend begins to emerge. The location of the peak is largely unaffected for moderate rotation rates, but a modest shift in location is observed at N = 3 due to the dominance of rotation in flows for N > 1. Scaling production with  $u_{\tau}^4/v$  yields inner-scaling, see Fig. 14d-f, and provides a reasonable collapse of the data near the wall, while an increase in production is noted towards the center of the flow. This peak is caused by the formation of peaks in normal Reynolds stresses  $< u_1u_1 >$  and  $< u_3u_3 >$  combined with increased mean velocity gradients due to the more parabolic profile induced by turbulence suppression, and corresponds to the peak in k shown in Fig. 10.

The magnitude of dissipation at the wall experiences an initial decrease as rotation is induced, followed by an increase for sufficiently high rotation rates, as shown in Fig. 15a-c. The value of N at which the minima occurs was not determined, but a Reynolds number dependence can be observed, with the minima occurring between N=0.5 and N=1 for Re=5,300 and between N=1 and N=3 for the higher Reynolds number cases. Figure 15d-f shows dissipation in inner-scaling and here three distinct regions can be seen, with the magnitude of  $\varepsilon$  increasing with increasing rotation in the near wall and center regions, but decreasing with increasing rotation in the mid-region. Inner-scaled  $\varepsilon$  begin to show collapse onto a single profile as Re is increased for the moderate rotation cases, but no such collapse is evident for N=3, again indicating a change in characterization of the flow from a pipe flow with rotation to a flow inside rotating cylinder with cross-flow as N increases beyond 1.

Dissipation at the wall is balanced by viscous diffusion, as shown in Fig. 16, where VD is given Eqn. (4). As with the peak in production, a shift in location of the trough in viscous diffusion is noted for the highest rotation rate. This shift towards the wall was also observed at N=2 by Orlandi and Ebstein[9] in their study of rotating flows at Re=4,900 (see Fig. 24c in the Appendix for a direct comparison). As with production and dissipation, a change in the characterization of the flow is evident at N=3 when viewing VD in inner-scaling, shown in Fig 16d-f, reinforcing the notion that the flow is now dominated by the flow inside a rotating cylinder regime.

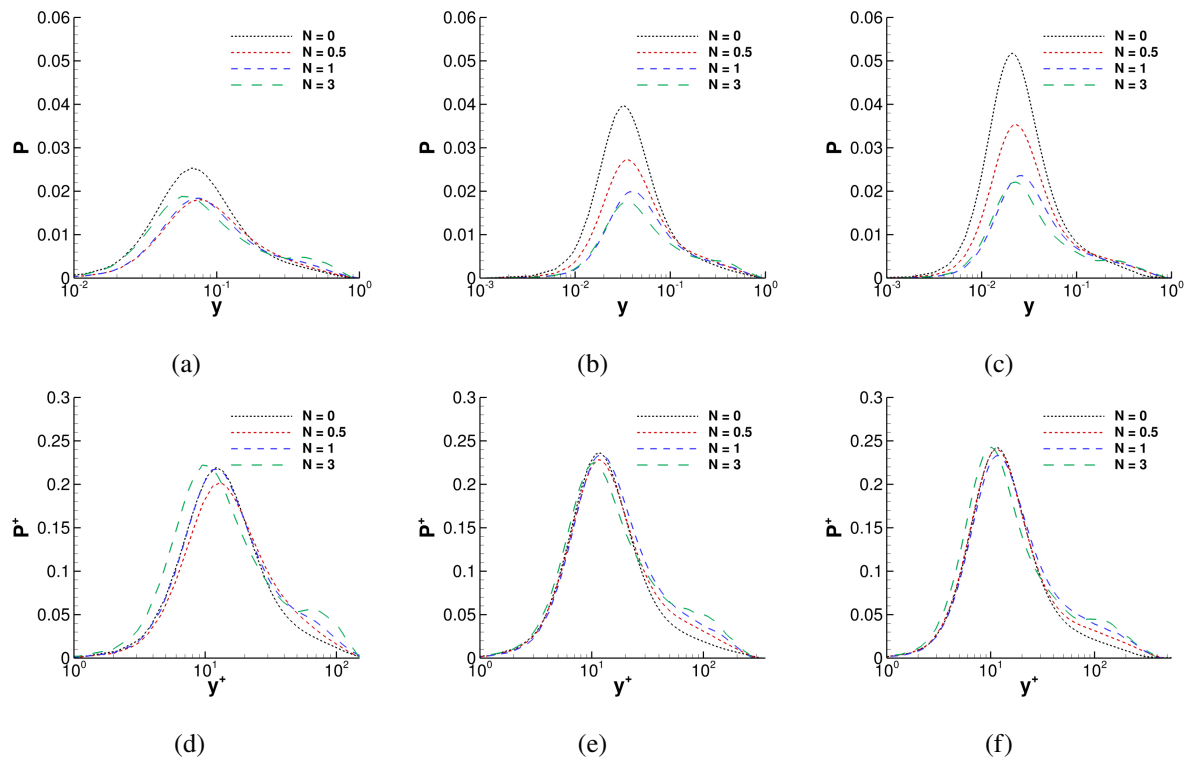


Fig. 14 Turbulent kinetic energy production for (a) Re = 5,300, (b) Re = 11,700, and (c) Re = 19,000. Inner-scaled production is presented in (d) Re = 5,300, (e) Re = 11,700, and (f) Re = 19,000.

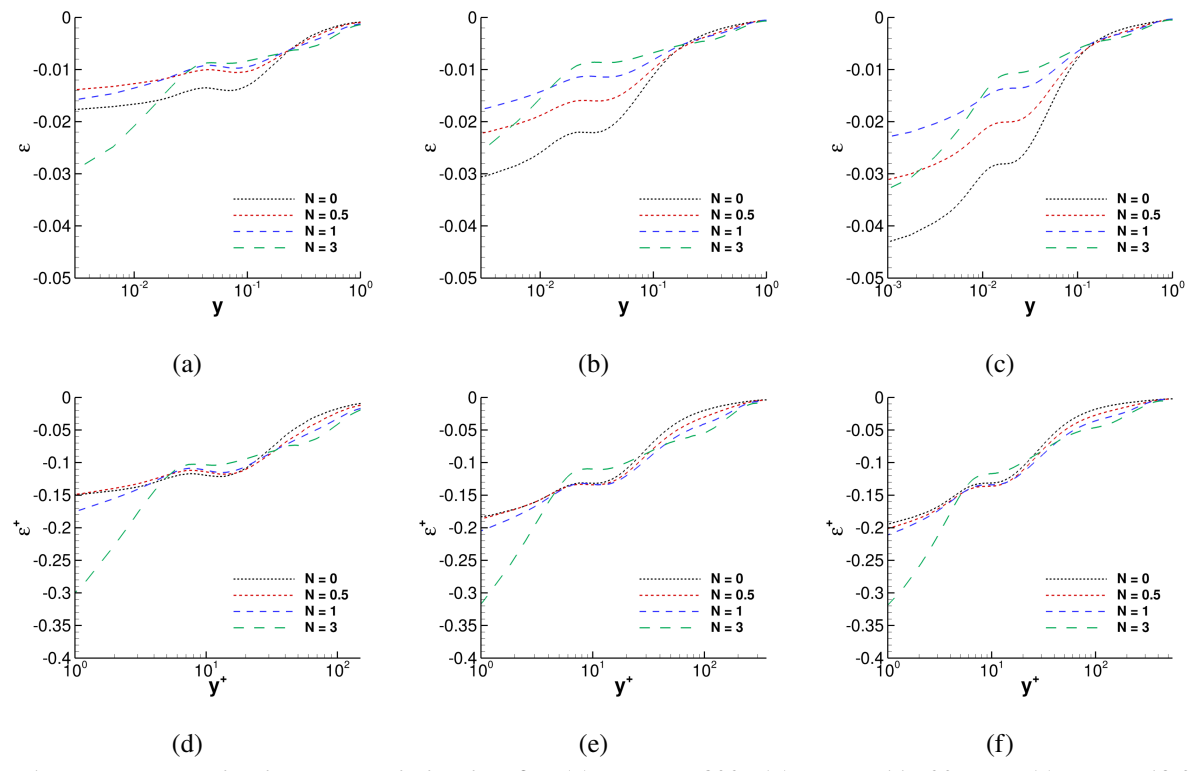


Fig. 15 Turbulent kinetic energy dissipation for (a) Re = 5,300, (b) Re = 11,700, and (c) Re = 19,000. Inner-scaled dissipation is presented in (d) Re = 5,300, (e) Re = 11,700, and (f) Re = 19,000.

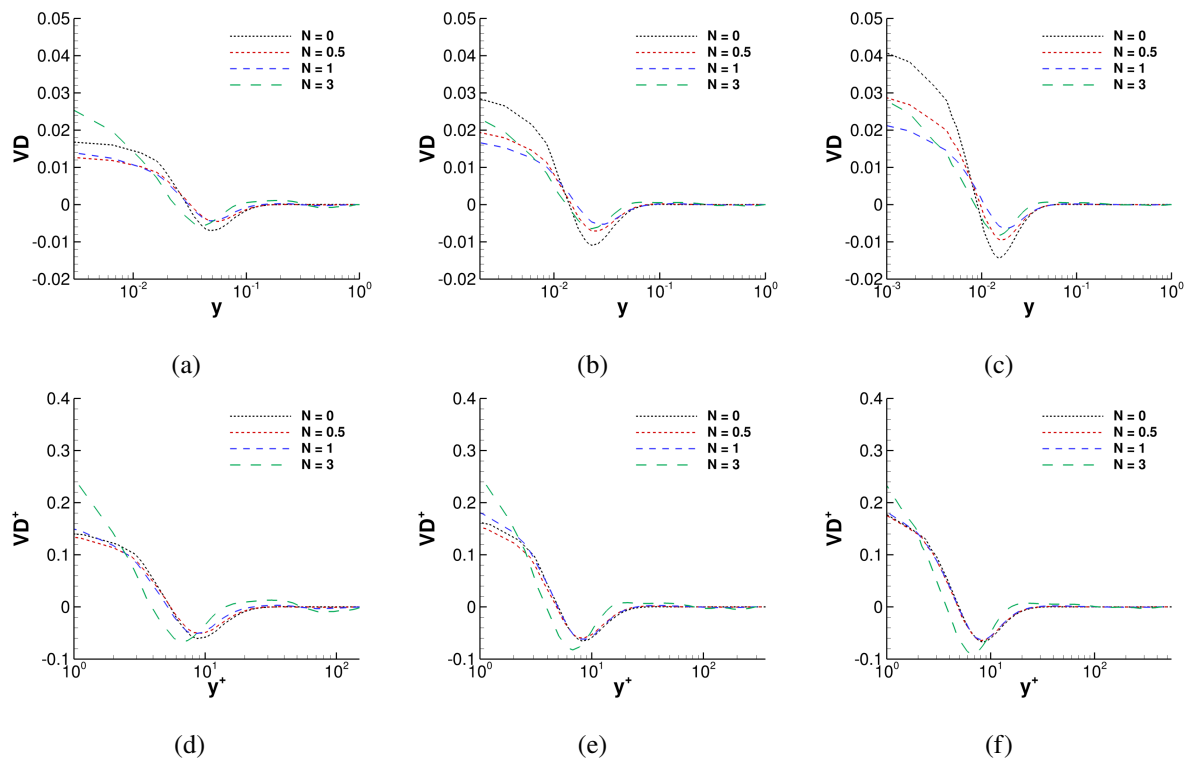


Fig. 16 Viscous diffusion for (a) Re = 5,300, (b) Re = 11,700, and (c) Re = 19,000. Inner-scaled viscous diffusion is presented in (d) Re = 5,300, (e) Re = 11,700, and (f) Re = 19,000.

Turbulent diffusion is given by Eqn. (5) and shown in Fig. 17a-c. The near wall peak in TD diminishes with increasing rotation, and is completely absent for  $Re = 5300 \ N = 3$ . Unlike the previous budget terms, inner-scaled turbulent diffusion does not completely collapse at moderate rotation rates, even at the highest Reynolds number, with a notable difference between the magnitude of the minimum value for the moderate rotation rates (N = 0.5 and 1) and the non-rotating case. The source of this difference has not been identified, though Reynolds number dependence cannot be ruled out. As with the previously mentioned budget terms, the behavior of N = 3 flows show a marked difference to flows at moderate rotation rates, again indicating dominance of the rotating regime. The high rotation number case shows both an increase in the magnitude of the minimum and a shift in the peak closer to the wall. This behavior matches well with observations by Orlandi and Ebstein [9] for N = 2 (see Fig. 24e in the Appendix).

Pressure diffusion, given by Eqn. (6), shows significant dependence on rotation number, with the increase in centrifugal force driving a moderate increase in the peak for rotation rates N=0.5 and N=1, as well as a substantial increase when N is increased to 3, as shown in Fig. 18a-c. The increase in the near-wall region remains evident even in inner-scaling, though it does show a decrease with increasing Reynolds number, indicating that the profiles of  $PD^+$  at moderate rotation numbers may stay close together at sufficiently high Re. At N=3, however, PD experiences a sharp increase that, like discrepancies noted in other turbulent budget terms, likely arises from the dominance of the rotating cylinder regime.

The analysis of turbulent kinetic energy budgets as a whole shows several trends emerging. Inner-scaling provides a reasonable collapse of most budget terms when applied to the Re = 19,000 flows at rotation numbers of  $N \le 1$ , with notable exceptions being a small region of increase in production away from the wall and differences in the minimum in turbulent diffusion and the maximum in pressure diffusion. Although it may be speculated that collapse at higher Reynolds numbers than those studied here is still possible. However, notable evidence for a change in behavior of the flow at N > 1 is observed in inner-scaling, with features such as, the peaks in production, viscous diffusion, and turbulent diffusion shifting closer to the wall, and large differences in maxima and minima values of each budget term when compared to pipe flow with  $N \le 1$ . These trends for N = 3 correspond well with data collected by Orlandi and Ebstein [9] at Re = 4,900 and N = 2, and serve to reinforce the notion that high N flows are dominated by rotation and cannot be adequately characterized by "classical" pipe flow characteristics.

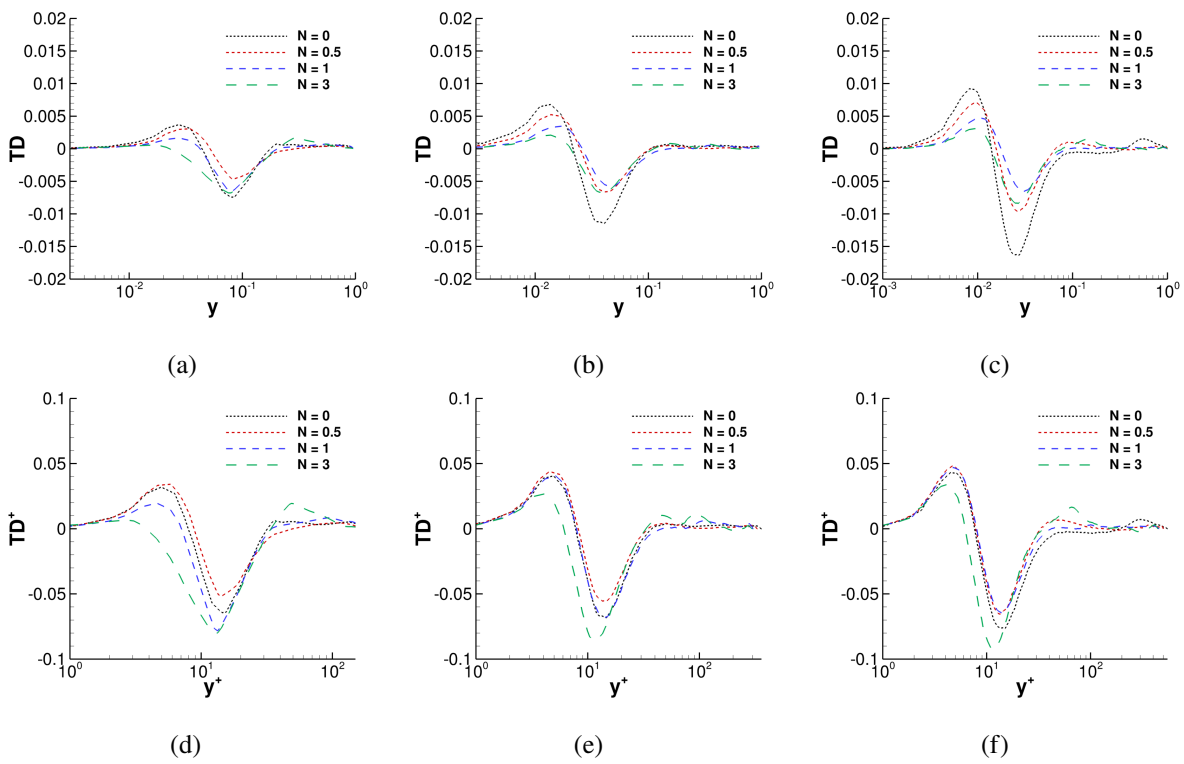


Fig. 17 Turbulent diffusion for (a) Re = 5,300, (b) Re = 11,700, and (c) Re = 19,000. Inner-scaled turbulent diffusion is presented in (d) Re = 5,300, (e) Re = 11,700, and (f) Re = 19,000.

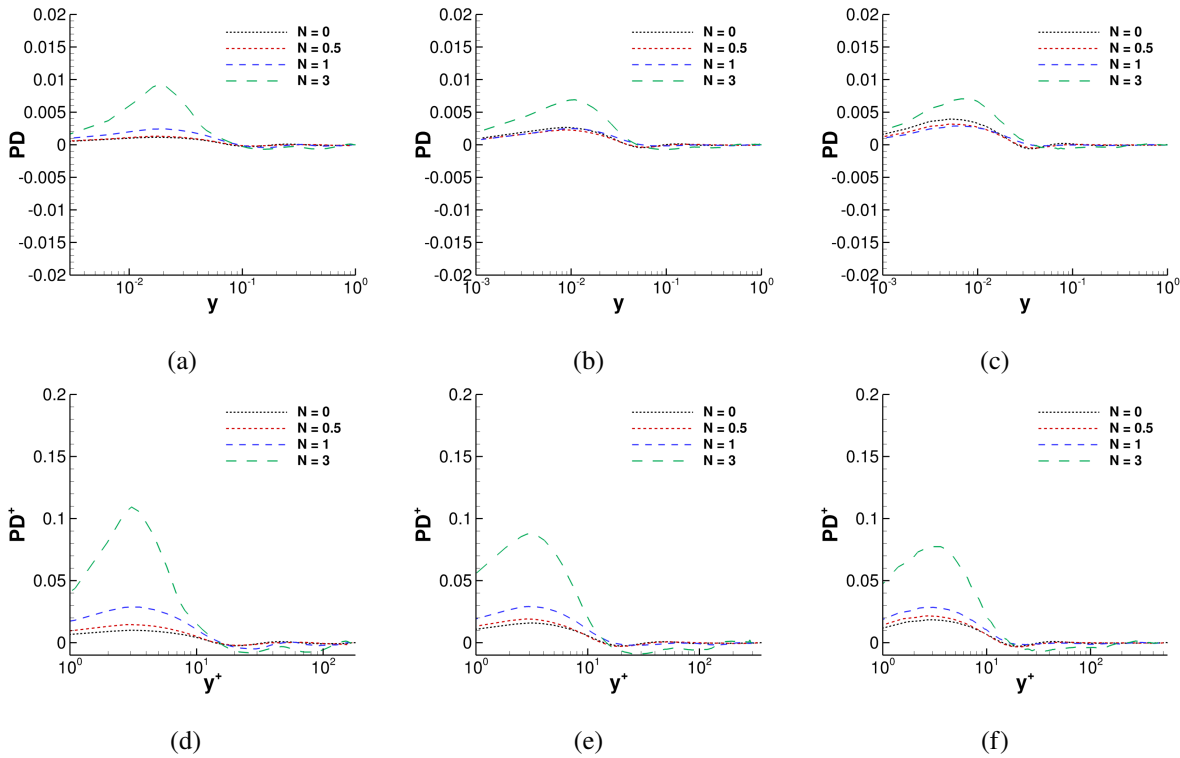


Fig. 18 Pressure diffusion for (a) Re = 5,300, (b) Re = 11,700, and (c) Re = 19,000. Inner-scaled pressure diffusion is presented in (d) Re = 5,300, (e) Re = 11,700, and (f) Re = 19,000.

# **IV. Conclusions**

Highly-resolved DNS of rotating pipe flow were conducted at Reynolds numbers Re = 5,300, 11,700, and 19,000 at rotation rates N = 0, 0.5, 1, and 3. Mean velocities, Reynolds stresses, turbulent kinetic energy, and turbulent kinetic energy budgets were analyzed to study the phenomenon of turbulence suppression. Relations between mean streamwise velocity and rotation number were found to be consistent with experimental data, and drag reduction was observed for each rotating case. By analyzing turbulent kinetic energy, a metric was defined to quantify turbulence suppression by normalizing the integral of turbulent kinetic energy by the total mean kinetic energy. This metric provides an easily computable and consistent means to identify turbulence suppression in rotating pipe flows that aligns well with the current definition of the phenomenon. Finally, inner-scaling was shown to work well in collapsing turbulent kinetic energy budget terms to a single profile for rotation numbers up to N = 1, but flows at higher rotation rates to be characteristic of pipe flow and are dominated by the flow inside a rotating cylinder regime.

# **Appendix**

Normal Reynolds stresses as well as Reynolds Shear stress for the non-rotating cases were compared to previous DNS data from a study conducted by Khoury *et al.*[19] and are presented in Fig. 19 in cylindrical coordinates. Reynolds stresses for all cases, both rotating and non-rotating are presented in cylindrical coordinates in Fig. 20 for  $\langle u_z u_z \rangle^+$ , Fig. 21 for  $\langle u_r u_r \rangle^+$ , Fig. 22 for  $\langle u_\theta u_\theta \rangle^+$ , and Fig. 23 for  $\langle u_z u_r \rangle^+$ .

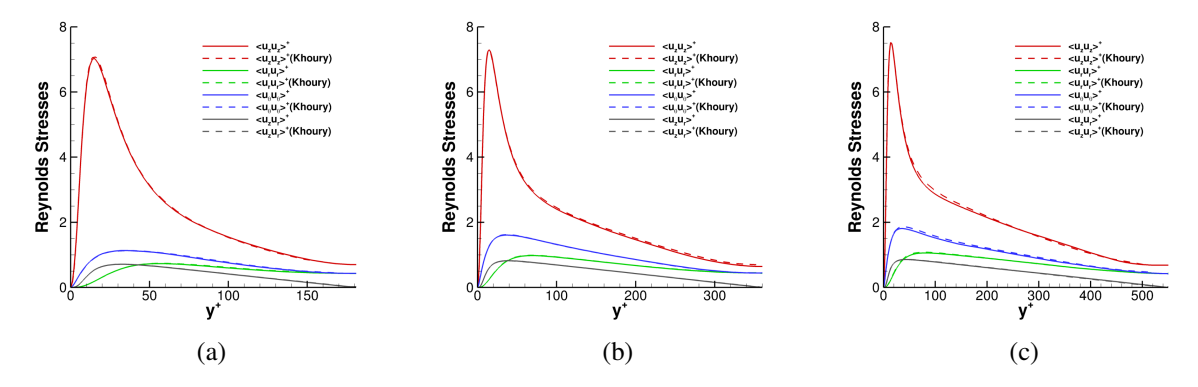


Fig. 19 Comparison of inner-scaled Reynolds stresses to data by Khoury *et al.*[19] for (a) Re = 5,300, (b) Re = 11,700, and (c) Re = 19,000.

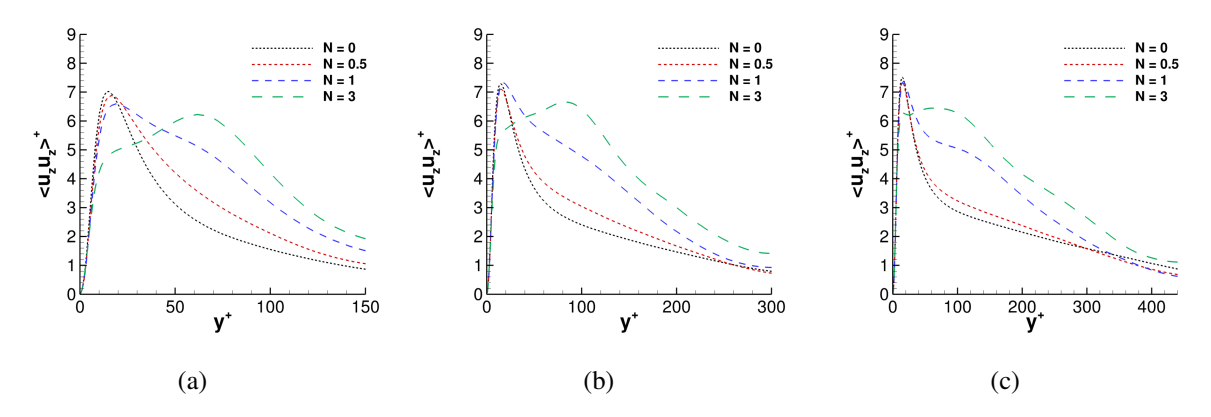


Fig. 20 Streamwise normal Reynolds stress normalized by  $u_{\tau}^2$  for (a) Re = 5,300, (b) Re = 11,700, and (c) Re = 19,000.

DNS of rotating flows at the Reynolds numbers presented in this paper had not been previously conducted, therefore TKE budget terms were validated by comparing values for Re = 5,300 with data from the studies conducted by Orlandi and Ebstein[9] at Re = 4,900, as presented in Fig. 24.

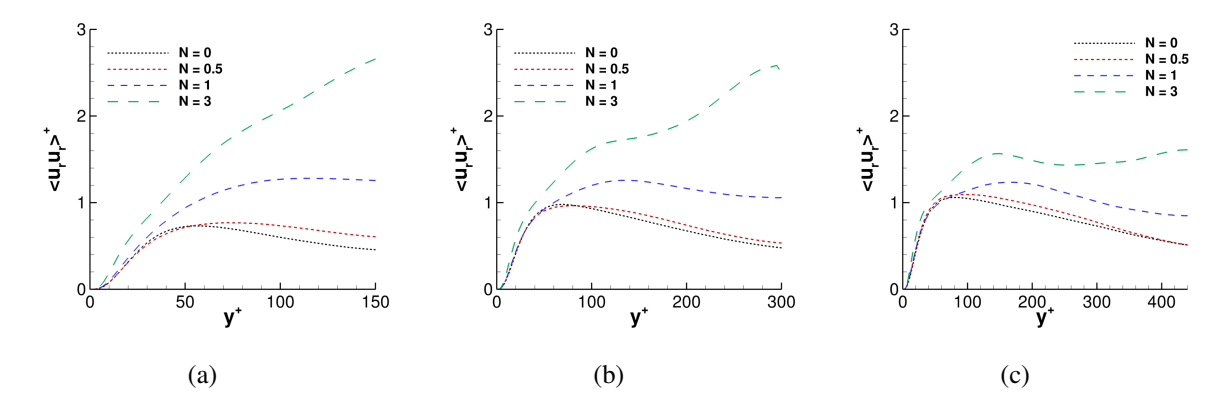


Fig. 21 Radial normal Reynolds stress normalized by  $u_{\tau}^2$  for (a) Re = 5,300, (b) Re = 11,700, and (c) Re = 19,000.

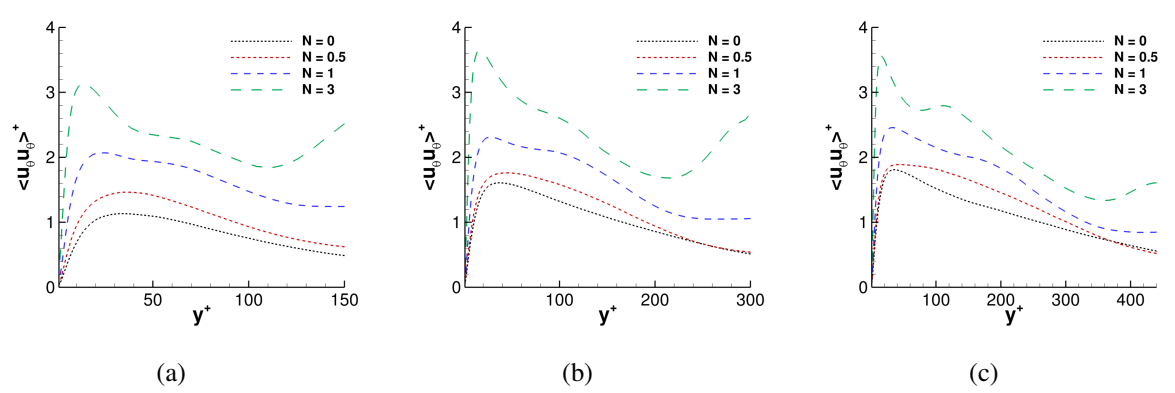


Fig. 22 Azimuthal normal Reynolds stress normalized by  $u_{\tau}^2$  for (a) Re = 5,300, (b) Re = 11,700, and (c) Re = 19,000.

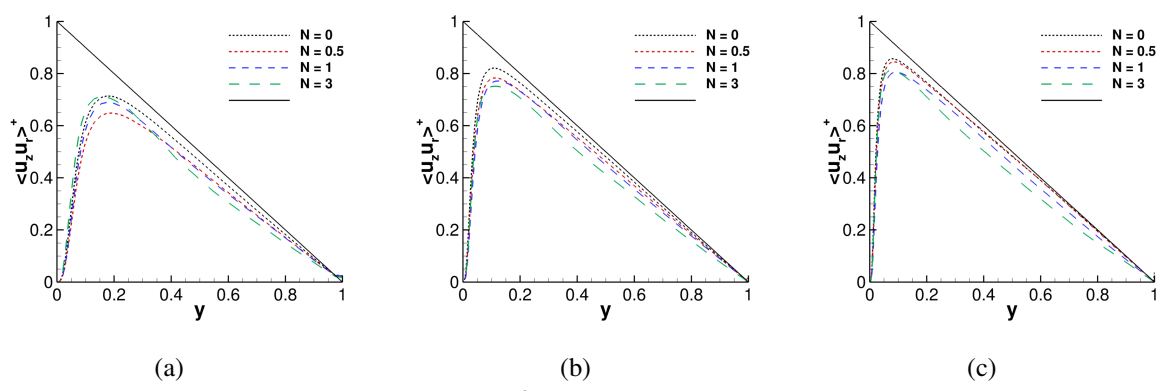


Fig. 23 Reynolds shear stress normalized by  $u_{\tau}^2$  for (a) Re = 5,300, (b) Re = 11,700, and (c) Re = 19,000.

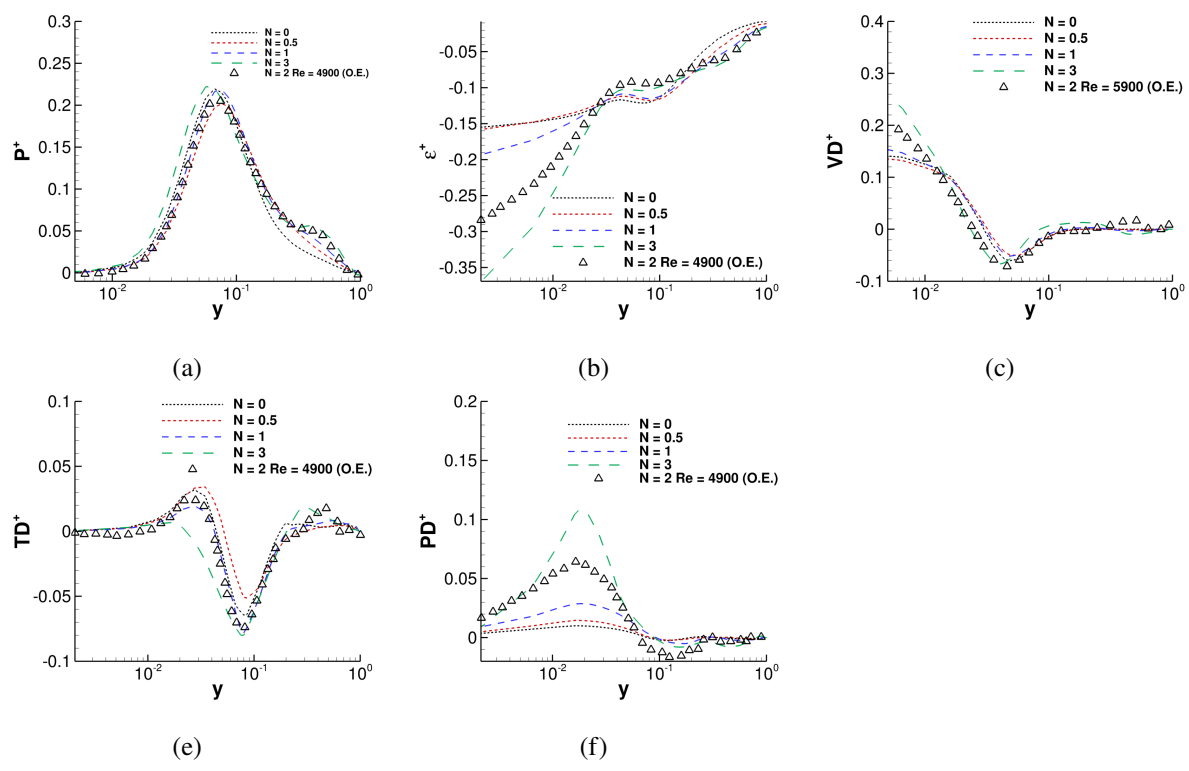


Fig. 24 Comparison of turbulent kinetic energy budget terms for Re = 5,300 with DNS data from Orlandi & Ebstein[9] at Re = 4,900.

# Acknowledgments

This work was supported by funding from the National Science Foundation under award CBET-1706346 with Dr. R. Joslin as Program Manager.

This research is part of the Blue Waters sustained-petascale computing project, which is supported by the National Science Foundation (awards OCI-0725070 and ACI-1238993) and the state of Illinois. Blue Waters is a joint effort of the University of Illinois at Urbana-Champaign and its National Center for Supercomputing Applications.

This work used the Extreme Science and Engineering Discovery Environment (XSEDE), which is supported by National Science Foundation grant number ACI-1548562[20]. Research was conducted using the Stampede2 and Comet HPC systems through allocation TG-CTS180008.

#### References

- [1] Narasimha, R., and Sreenivasan, K., "Relaminarization of fluid flows," *Advances in Applied Mechanics*, Vol. 19, 1979, pp. 221–309.
- [2] White, A., "Flow of a fluid in an axially rotating pipe," *Journal of Mechanical Engineering Science*, Vol. 6, No. 1, 1964, pp. 47–52.
- [3] Murakami, M., and Kikuyama, K., "Turbulent flow in axially rotating pipes," *Journal of Fluids Engineering*, Vol. 102, No. 1, 1980, pp. 97–103.
- [4] Kkikuyama, K., Murakami, M., Nishibori, K., and Maeda, K., "Flow in an Axially Rotating Pipe: A calculation of flow in the saturated region," *Bull. JSME*, Vol. 26, No. 214, 1983, pp. 506–513.
- [5] Nishibori, K., Kikuyama, K., and Murakami, M., "Laminarization of turbulent flow in the inlet region of an axially rotating pipe." *JSME International Journal*, Vol. 30, No. 260, 1987, pp. 255–262.
- [6] Reich, G., and Beer, H., "Fluid flow and heat transfer in an axially rotating pipe I. Effect of rotation on turbulent pipe flow," *International Journal of Heat and Mass Transfer*, Vol. 32, No. 3, 1989, pp. 551–562.
- [7] Feiz, A., Ould-Rouis, M., and Lauriat, G., "Turbulence statistics in a fully developed rotating pipe flow," *Journal of Enhanced Heat Transfer*, Vol. 12, No. 3, 2005.
- [8] Orlandi, P., and Fatica, M., "Direct simulations of turbulent flow in a pipe rotating about its axis," *Journal of Fluid Mechanics*, Vol. 343, 1997, pp. 43–72.
- [9] Orlandi, P., and Ebstein, D., "Turbulent budgets in rotating pipes by DNS," *International Journal of Heat and Fluid Flow*, Vol. 21, No. 5, 2000, pp. 499–505.
- [10] Orlandi, P., and Fatica, M., "Direct simulations of turbulent flow in a pipe rotating about its axis," *Oceanographic Literature Review*, Vol. 7, No. 45, 1998, p. 1257.
- [11] Borchetta, C., Brehm, C., and Bailey, S., "On the Development of an Apparatus to Examine Rotating Pipe Flow at High Rotation Numbers," *APS DFD*, 18-20 November, Atlanta, 2018.
- [12] Bradshaw, P., "The analogy between streamline curvature and buoyancy in turbulent shear flow," *Journal of Fluid Mechanics*, Vol. 36, No. 1, 1969, pp. 177–191.
- [13] Davis, J., Ganju, S., and Brehm, C., "Direct Numerical Simulations of Turbulence Suppression in Rotating Pipe Flows," *Parallel CFD Conference Proceeding, May 14-18, Indianapolis, Indiana*, 2018.
- [14] Davis, J., Ganju, S., and Brehm, C., "Direct Numerical Simulations of Rotating Turbulent Pipe Flows at Moderate Reynolds Numbers," *APS DFD*, *18-20 November*, *Atlanta*, 2018.
- [15] Brehm, C., Davis, J., Ganju, S., and Bailey, S., "A Numerical Investigation of the Effects of Rotation on Turbulent Pipe Flows," 11th International Symposium on Turbulence and Shear Flow Phenomena (TSFP11) Southampton, UK, July 30 to August 2, 2019, 2019.
- [16] Ashton, N., Davis, J., and Brehm, C., "Assessment of the Elliptic Blending Reynolds Stress Model for a Rotating Turbulent Pipe Flow Using New DNS Data," *AIAA Aviation and Aeronautics Forum and Exposition Dallas, TX, June 17 to June 21*, 2019. AIAA Paper 2019.

- [17] Ashton, N., and Stoellinger, M. K., "Computation of Turbulent Flow in a Rotating Pipe using the Elliptic Blending Reynolds Stress Model," *46th AIAA Fluid Dynamics Conference*, No. June, 2016, pp. 1–11. doi:10.2514/6.2016-3943, URL http://arc.aiaa.org/doi/10.2514/6.2016-3943.
- [18] Fischer, P. F., "An Overlapping Schwarz Method for Spectral Element Solution of the Incompressible Navier-Stokes Equations," *Journal of Computational Physics*, Vol. 133, 1997, pp. 84–101.
- [19] El Khoury, G. K., Schlatter, P., Noorani, A., Fischer, P. F., Brethouwer, G., and Johansson, A. V., "Direct numerical simulation of turbulent pipe flow at moderately high Reynolds numbers," *Flow, turbulence and combustion*, Vol. 91, No. 3, 2013, pp. 475–495.
- [20] Towns, J., Cockerill, T., Dahan, M., Foster, I., Gaither, K., Grimshaw, A., Hazlewood, V., Lathrop, S., Lifka, D., Peterson, G. D., Roskies, R., Scott, J., and Wilkins-Diehr, N., "XSEDE: Accelerating Scientific Discovery," *Computing in Science Engineering*, Vol. 16, No. 05, 2014, pp. 62–74. doi:10.1109/MCSE.2014.80.